# Sensitive integrated photonic transducer with predictive modeling for underwater ultrasound sensing

SABIJU VALIYA VALAPPIL, 1,\* D MARTIN VERWEIJ, 1 PETER HARMSMA, MAURITS VAN DER HEIDEN, 3 ANNE MAAIKE GERRITSMA, ROBERT ALTMANN, 2 AND PAUL VAN NEER<sup>3</sup>

**Abstract:** A high signal-to-noise ratio (SNR) is critical for sensitive ultrasound applications. Unlike traditional piezoelectric sensors that rely on material properties, an integrated photonic ultrasound transducer (IPUT) separates sensing and read-out systems, allowing for better optimization. Here we use a silicon Mach–Zehnder interferometer (MZI) embedded in a circular silicon dioxide membrane, where incident acoustic pressure modulates the optical phase. We extend the semi-analytical model introduced in our previous work to incorporate the device geometry and fabrication-induced internal stress, enabling accurate prediction of the transducer's optomechanical response. This approach resulted in an experimentally measured sensitivity of 0.47 pm/Pa at a resonance frequency near 1 MHz, in close agreement with the model prediction of 0.46 pm/Pa. This performance represents a sevenfold improvement over previously reported devices [Lienders et al., Sci. Rep., 2015]. Additionally, we have developed two more IPUTs where multiple membranes were cascaded and their performance was experimentally investigated. The IPUT with three membranes had an RTF of 1.4 pm/Pa, while the IPUT with five membranes' RTF was 2.24 pm/Pa. Our IPUTs also have excellent noise performance, as demonstrated by the noise equivalent pressure (NEP) of the device. NEP of IPUT with one membrane is 42.5 mPa, IPUT with three membranes is 15.5 mPa, and the IPUT with five membranes is 14.2 mPa. Compared to the state-of-the-art ultrasound sensors, our IPUT with five membrane shows 35 times lower NEP. Our results demonstrate that fabrication-aware modeling is crucial for achieving optimal sensitivity in IPUTs, establishing the proposed IPUT as a promising solution for underwater ultrasound sensing.

Published by Optica Publishing Group under the terms of the Creative Commons Attribution 4.0 License. Further distribution of this work must maintain attribution to the author(s) and the published article's title, journal citation, and DOI.

### Introduction

Medical imaging employs various technologies to visualize internal organs and diagnose diseases. It plays a crucial role in supporting medical diagnosis and detecting health issues [1]. The various medical imaging methods (imaging modalities) include diagnostic ultrasound [2], positronemission tomography [3], magnetic resonance imaging [4], cardiac electrical imaging [5], X-ray, and computed tomography, among others [6–8]. Ultrasound imaging is a commonly used medical

<sup>&</sup>lt;sup>1</sup>Faculty of Applied Sciences, Delft University of Technology, Lorentzweg 1, Delft, 2628 CJ, The Netherlands

 $<sup>^2</sup>$ Nederlandse Organisatie voor Toegepast Natuurwetenschappelijk Onderzoek (TNO), Stieltjesweg 1, Delft, 2628CK, The Netherlands

 $<sup>^3</sup>$ Nederlandse Organisatie voor Toegepast Natuurwetenschappelijk Onderzoek (TNO), Oude Waalsdorperweg 63, Den Haag, 2509JG, The Netherlands \*S.ValiyaValappil@tudelft.nl

imaging modality because acoustic measurement equipment is safe, operates in real-time, and is relatively inexpensive.

Transducers used in medical ultrasound imaging are commonly piezoelectric-based devices [9], capacitive micromachined ultrasound transducers (cMUTs) [10], or piezoelectric micromachined ultrasound transducers (pMUTs) [11]. Piezoelectric-based devices rely on principles of piezoelectricity (elastic deformation is induced in a piezoelectric crystal when it is subjected to an electric field, and vice versa). cMUTs and pMUTs are microelectromechanical systems in which a membrane is deformed by means of electrostatic forces and thin-film piezoelectric layers, respectively. Both pMUTs and cMUTs are based on complementary metal oxide semiconductor (CMOS) processes and are therefore ideally suited for high-volume manufacturing at low cost.

A high signal-to-noise ratio (SNR) is required to obtain a high image quality. However, safety regulations pose upper limits to the peak pressure (thereby the signal strength) of the acoustic pulse (mechanical index) and to the heat dissipation (thermal index) into the tissue [12]. Additionally, the pressure pulse returning from the tissue has a strongly reduced amplitude due to attenuative, diffraction-related, and scattering losses, which are all frequency-dependent. Thus, the transducers need a high receive transfer function (RTF) and/or a low noise floor. The noise equivalent pressure (NEP)—the pressure for which the SNR is unity—of all the aforementioned devices with a matrix array element of aperture size of  $0.5 \times 0.5$  wavelength<sup>2</sup> is in the order of 0.5 Pa per element when operating around 1 MHz with 80% - 6 dB bandwidth (BW) [10,13,14]. Piezomaterial/pMUT/cMUT-based transducers are limited by the noise in the receive chain, which is usually dominated by the noise figure of the first amplifier. The theoretical lowest noise floor would be determined by the Brownian motion of the particles [15] in the measuring medium and the thermal noise of the transducer. This noise level is much lower than the receive chain noise.

Integrated photonic ultrasound transducers (IPUTs) consist of a mechanical resonator coupled to an optical circuit. An incident acoustic wave excites the mechanical resonator and thus deforms the optical circuit, which changes its optical transfer function. Westerveld et al. [16] demonstrated that IPUTs have higher sensitivity (up to two orders of magnitude) per unit area than piezo-based devices. For instance, the piezoelectric matrix array presented by Xia et al., contains 25 elements of size 0.9 mmx0.9 mm with a central frequency of 0.9 MHz, and measured NEP of 0.5 Pa for a single array element [13]. A similar IPUT provided by Leinders et al. with 0.76 MHz central frequency has an NEP of 0.4 Pa while the diameter of the sensor was 124 µm [17]. In other words, the IPUT demonstrated a similar NEP as the piezo element for a sixty times lower surface area. Thus, for the same cross-sectional area, IPUTs can outperform piezoelectric ultrasound transducers. The optical circuit of an IPUT can be configured to be part of an interferometric or optical resonator-based read-out. The optical resonators can be classified as Fabry-Perot etalons [18], whispering gallery mode (WGM) microcavities [17], and Bragg gratings [19]. The incoming ultrasound causes the optical resonance frequencies to shift in these resonators. The shift can then be read out with high accuracy by using a laser at a wavelength where the slope of the resonance curve is maximum. In IPUTs based on Mach-Zehnder interferometers (MZIs) [20], an optical probe signal is split to a sensing path and a reference path. Both paths are recombined, so that they can interfere. The sensing arm is placed on the mechanical resonator. The incoming pressure induces an optical phase change in the sensing arm, resulting in a detectable output signal. Compared to optical-resonator-based devices, MZIs possess unique advantages as their operation mechanism is based on interferometry. The dynamic range of the MZI is virtually infinite as compared to RRs and other WGM devices [21]. Other advantages include constant and scalable sensitivity, i.e., it increases linearly with the spiral length, no directional ambiguity, and only needs a simple interrogation system. Additionally, the optical wavelength of the laser source does not need extremely precise alignment as the transmission intensity varies linearly as compared to the sudden change in intensity of RRs [21].

Several studies have described IPUTs with high sensitivity and low noise levels [22-24]. Hornig et al. proposed an ultrasound sensor operating in air and water possessing a broad (5 MHz) BW with a noise floor close to its thermal noise. They used amorphous silicon on a silicon dioxide platform to create buckled dome cavity resonators (Fabry-Perot etalon) to achieve high finesse (ratio of full-width half-maximum bandwidth to the free spectral range representing the steepness of the optical resonance peak) and low noise [22]. The fabrication is performed by controlled buckling (via heating) of multiple layers, which is a complicated process. For instance, the heating can result in the decomposition of the intermediate layer, leading to delamination [25]. Yang et al. proposed a highly sensitive air-coupled ultrasound sensor based on WGM microcavities with a BW of 2.7 MHz where microtoroids were used to obtain high optical and mechanical Q-factors, resulting in noise levels close to the sensor's thermal noise [23]. They also developed a WGM microdisk ultrasound sensor whose sensitivity was improved by tuning the disk geometry [24]. To that end, they exploited the flapping mode (mechanical deformation) of the microdisk to enhance the ultrasound response and improve the sensitivity. Both the aforementioned devices operate in the air and have high mechanical Q factors (around 700), while the microdisk sensor operates at relatively low frequencies (less than 100 kHz). Westerveld proposed a high-sensitivity broadband optomechanical sensor based on RRs with 27 MHz BW [16]. However, the fabrication is complicated due to the strict requirement of a tiny air gap (15 nm) in the ring. Sun et al. proposed an optical microring-based ultrasound detector with 103 MHz BW, where the rings were placed on a multicore fiber facet [26]. Fan et al. proposed an ultrasound sensor based on an in-fiber dual-cavity Fabry-Perot etalon having a broad BW (tens of megahertz) [27]. These devices do not utilize the dynamic influence of the mechanical components, thus lacking mechanical resonance-induced sensitivity enhancements and therefore have limited sensitivity. This concept is manufacturable with current silicon photonic integration technologies making the IPUT a sensitive and feasible concept for ultrasonic sensing Ouyang et al. developed an MZI-based photonic ultrasound sensor that operates in water (which is a medium comparable to tissues), where a waveguide spiral is placed on a square membrane at mechanical resonance operating at 0.47 MHz with an NEP of 0.38 Pa [20,28]. Leinders et al. proposed an RR-based ultrasound sensor, which also operates in water with an NEP of 0.4 Pa [17,29]. Both these devices operates at narrow BWs (approximately  $20\% - 6 \,\mathrm{dB}$ ).

Although there are several experimental works present in IPUTs, there are limited studies on their modeling aspects. Tsesses et al. proposed a modeling approach to analyze the photonic ultrasound detectors where different acoustic wave types, waveguide dimensions, and polarizations were included [30]. The modeling was based on the static response of the waveguide strip, which can have accuracy issues while predicting the response in a dynamic setting. Rochus et al. proposed an analytical model to analyze the photonic ultrasound sensor including mechanical nonlinearities and optical losses [31,32]. Although it allows fast computation, the formulation still relies on the static response of the membrane and can lead to inaccurate predictions for vibrating membranes (especially close to resonance). To the best of our knowledge, no studies have modeled the dynamic response of photonic ultrasound transducers capturing the vibration of the mechanical resonator.

In this work, we extend the semi-analytical model developed in our previous work [33] by incorporating the influence of the actual device geometry and internal stress developed during fabrication to design an MZI-based IPUT; fabricate it, and compare its experimental performance obtained in a water tank to the aforementioned model. We further develop similar IPUTs with multiple membranes and investigate their dynamic response experimentally.

#### 2. Theory

We begin by describing the IPUT and its operation as shown in Fig. 1. Here, we focus on an MZI-based IPUT, which comprises two long optical waveguides arranged in the form of spirals,

where one is referred to as the sensing arm (the spiral sitting on the dark blue membrane) and the other as the reference arm. The incoming laser power is split equally between these two arms by a splitter, while the coupler recombines the signals. Due to interference, the output signal varies sinusoidally with the phase difference between the two arms, as shown by the blue curve in the transmission-wavelength plot of the same figure. The static phase difference  $\Delta \phi$  is given by [34]:

$$\Delta \phi = \frac{2\pi n_{\text{eff}} \Delta L}{\lambda},\tag{1}$$

where  $n_{\rm eff}$  is the optical effective index of the waveguides,  $\Delta L$  is the fabricated difference in the arm length (path length difference), and  $\lambda$  is the optical wavelength. The static arm length difference is 170  $\mu$ m, which is sufficiently large to characterize the MZI response by sweeping the laser wavelength over the free spectral range (FSR=4 nm), and sufficiently small to avoid any performance degradation due to laser wavelength noise. Incoming ultrasound excites the membrane at or close to its resonance, dynamically modifying the length, cross-sectional geometry, and induced stresses of the optical waveguide in the sensing arm. These changes cause variations in the output optical transmission of the sensing arm, and the transmission intensity at the operational wavelength is varied by an amount  $\Delta T$ , which is measured using an optical detector.

#### 2.1. Optomechanical interactions of the IPUT

A change in the incoming pressure dP induces a phase change  $d\phi$  and an amplitude change dA between the sensing arm and the reference arm of the MZI. This is due to the fact that the effective refractive index  $n_{\rm eff} = n_{\rm eff}(\lambda, P)$  is a function of the applied wavelength  $\lambda$  and the pressure P (through the induced straining of the material), while the arm length L = L(P) is also a function of the pressure (through the induced length change). Since the change in the amplitude is much smaller than that of the phase change, we omit its influence hereafter. The applied wavelength is fully determined by the laser and not influenced by the pressure. As a consequence, we find

$$\frac{d\phi}{dP} = \frac{d}{dP} \left( \frac{2\pi n_{\text{eff}} L}{\lambda} \right) = \frac{2\pi}{\lambda} \left( n_{\text{eff}} \frac{dL}{dP} + L \frac{dn_{\text{eff}}}{dP} \right)$$
 (2)

In the context of this work, we characterize the IPUT by its wavelength-dependent transmission, see Fig. 1. For a fixed value of  $\lambda$ , a pressure change  $\Delta P$  will cause a change of transmission  $\Delta T$ . To keep the transmission at the same value as before applying the change  $\Delta P$ , we may shift the wavelength over a distance  $\Delta \lambda$ . The receive transfer function (RTF) is defined as the wavelength shift  $\Delta \lambda$  that will exactly compensate the effects of a pressure change  $\Delta P$  on the transmission. This implies that the phase should remain the same, i.e.,

$$\phi(\lambda + \Delta\lambda, P + \Delta P) = \phi(\lambda, P). \tag{3}$$

Using the first-order Taylor approximation of the left-hand term, Eq. (3) can be written as

$$\phi(\lambda, P) + \Delta \lambda \frac{d\phi}{d\lambda} + \Delta P \frac{d\phi}{dP} = \phi(\lambda, P). \tag{4}$$

This implies that

$$\Delta \lambda \frac{d\phi}{d\lambda} = -\Delta P \frac{d\phi}{dP},\tag{5}$$

from which the RTF follows as:

$$\frac{\Delta\lambda}{\Delta P} = -\frac{d\phi}{dP}\frac{d\lambda}{d\phi}.$$
 (6)

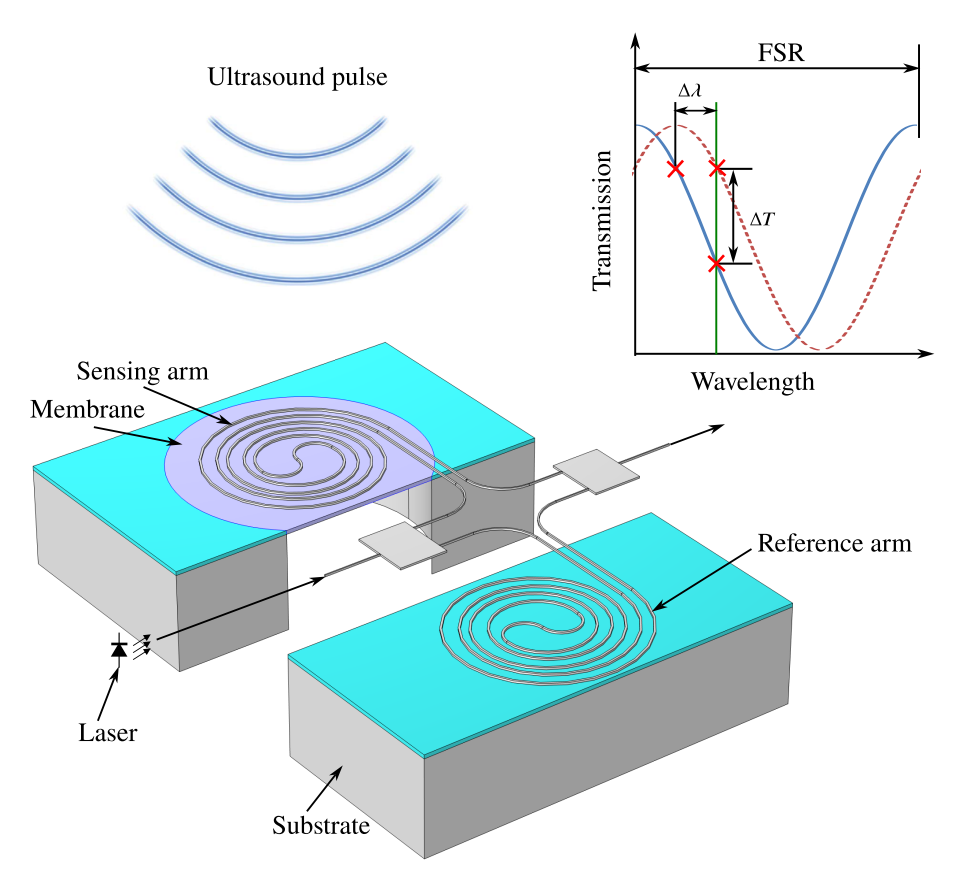


**Fig. 1.** Schematic representation of an MZI-based IPUT device. The sensing arm is located on a  $\mathrm{SiO}_2$  membrane, the reference arm is situated on the silicon substrate. An incoming ultrasound pulse excites the membrane in its resonance mode, leading to an optical phase shift in the sensing arm. Optical interference in the optical combiner leads to a change in output power at the laser wavelength (C-band, near 1550 nm). The plot shows the transmission intensity as a function of the optical wavelength for the MZI without (blue solid curve) and with (red dashed curve) the presence of an ultrasound pulse. FSR is the free spectral range, while  $\Delta\lambda$  and  $\Delta T$ , respectively, indicate the change in the wavelength and transmission due to the incoming ultrasound pulse for a fixed transmission or wavelength.

Because the arm length L does not depend on the wavelength of the laser, we find

$$\frac{d\phi}{d\lambda} = \frac{d}{d\lambda} \left( \frac{2\pi n_{\text{eff}} L}{\lambda} \right) = 2\pi L \left( \frac{-n_{\text{eff}}}{\lambda^2} + \frac{(dn_{\text{eff}}/d\lambda)}{\lambda} \right) = \frac{2\pi n_g L}{\lambda^2},\tag{7}$$

in which  $n_g = \left(n_{\rm eff} - \lambda \frac{dn_{\rm eff}}{d\lambda}\right)$ , is the group refractive indices of the waveguide. Combining Eqs. (2), (6), and (7) yields for the RTF

$$\frac{\Delta \lambda}{\Delta P} = \frac{\lambda}{n_g L} \left( n_{\text{eff}} \frac{dL}{dP} + L \frac{dn_{\text{eff}}}{dP} \right). \tag{8}$$

## 3. Experimental setup

## 3.1. Experimental procedure

The schematic of the experimental setup, along with the list of equipment to characterize the RTF and NEP of the IPUT, is shown in Fig. 2. We separate the setup into optical and acoustical parts for convenience. The optical part contains a tunable laser, which emits light around 1550 nm (C-band). The light is passed through an in-fiber polarization controller. The latter ensures the light properly propagates through the IPUT since the IPUT only allows one polarization state. This light is coupled to the IPUT's optical circuit via an optical fiber array connected to the facet of the chip using a custom-fabricated optical glue and is modulated by the incoming ultrasound. The light coming out of the MZI is measured by a photodetector. After the signal is amplified at the trans-impedance amplifier, it is separated into AC and DC outputs before the analog-digital converter (ADC). The AC signal is used to measure the ultrasound signal, while the DC signal is used to characterize the spectrum of the IPUT's optical circuit and can be used for signal reconstruction and to optimize visibility.

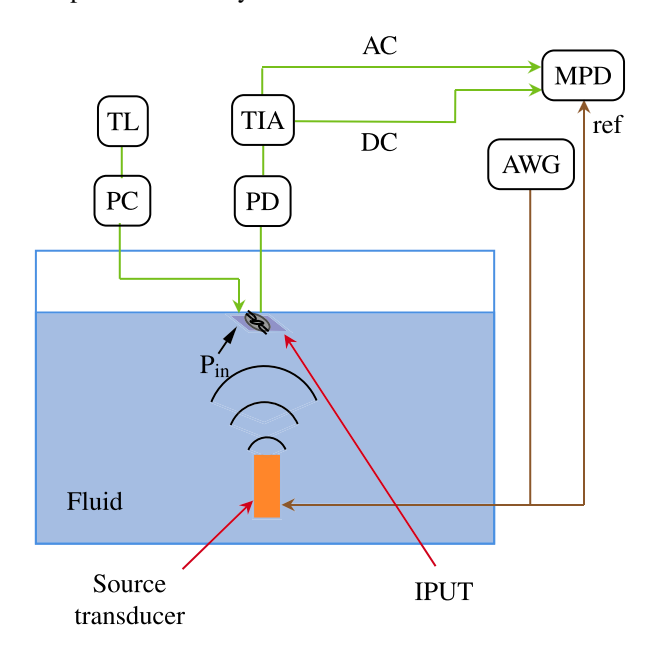


**Fig. 2.** Schematic of the experimental setup for ultrasound testing of IPUT submerged in water. The source transducer is Panametrics V303. Abbreviations and corresponding hardware – AWG: Waveform generator (Keysight 3321A), TL: Laser (EXFO T100SHP), PC: Polarization controller (Thorlabs FPC03), PD: Photodetector (Thorlabs DET10C2), TIA: Amplifier (FEMTO DHCA-100), and MPD: Digitizer (Spectrum M2i-4964-exp), which is an analog-to-digital converter (ADC).

Subsequently, we describe the acoustical part. The location of the source transducer is such that the IPUT is at the natural focus of the transducer. The distance between the IPUT and the transducer is approximately 29 cm. A photograph of the experimental setup is shown in Fig. 3(a). The water tank is filled with tap water. An arbitrary waveform generator generates a voltage signal corresponding to the desired waveform. This signal is sent to the ultrasound transducer, which produces the pressure wave. The source transducer (Panametrics V303) was calibrated before the start of the experiment using a pulse-echo measurement via a needle hydrophone [35], and has a central frequency of 0.975 MHz and a BW of 0.88 MHz (90 % -6 dB). To ensure maximum transmission between the transducer and IPUT, they are aligned along the propagation

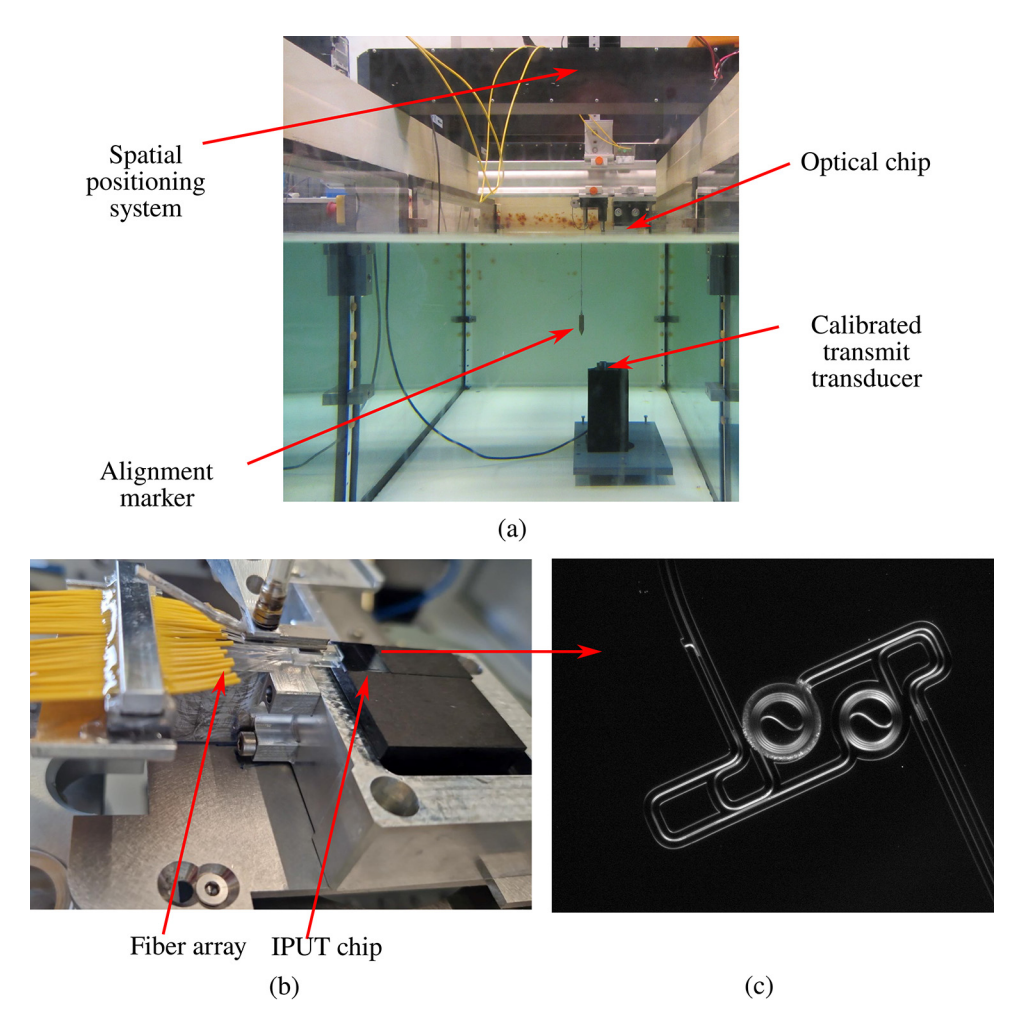


**Fig. 3.** Photographs of the experimental setup and IPUT chip. (a) The transmit transducer immersed in the water tank supplies an ultrasound pulse that excites the optical chip, which modifies its optical transfer function. (b) The laser source is connected to the IPUT chip, which contains several individual IPUTs via an optical fiber array. (c) The zoomed-in view of the photograph of the fabricated MZI-based IPUT chip, where the spirals in the sensing and reference arms contain 4 loops each. The MZI has three output channels at a  $\frac{2\pi}{3}$  phase difference.

axis. To that end, an alignment marker and a three-way (x - y - z) spatial positioning system are used (shown in the same figure). A broadband  $(100\% - 6\,\mathrm{dB})$  single sinusoid acoustic pulse with the central frequency around 1 MHz generated by the source transducer travels through the water to impinge on the IPUT, which modulates the phase of the light in the sensing arm of the MZI. This modulation is interrogated optically and digitized via a photodetector, amplifier, and digitizer chain as described in the previous paragraph.

#### 3.2. IPUT device description

The packaged IPUT device is shown in Fig. 3(b), while the photograph of the device with a single membrane is displayed in Fig. 3(c). We also tested multiple cascaded IPUTs containing three and five membranes (photograph not shown here but is similar to Figure 3(c)). The fiber

array is attached to the IPUT with a low-shrink UV and temperature-curable optical glue, while a custom-fabricated backing structure is used to limit the spurious acoustical reflections. The  $SiO_2$  membrane has a radius of  $60 \, \mu m$  and thickness of  $3 \, \mu m$ . A  $2 \, \mu m$  by  $3 \, \mu m$  (width by thickness) multi-mode silicon waveguide is used to create the spirals with four loops for the MZI, where only the fundamental mode is excited [36].

#### 4. Experimental results

## 4.1. Dynamic response of the IPUT

The dynamic response from the IPUT is obtained as an AC voltage at the input of the digitizer shown in Fig. 4(a), where a sampling rate of 30 MHz is used. The digitizer also recorded the signal exciting the source transducer. Using fast Fourier transform (FFT), both the input signal and output response are transformed to the frequency domain as shown in Fig. 4(b). The acoustic input pulse arriving at the IPUT will be different than the supplied signal to the source transducer (dashed curve) due to the transfer function of the transducer, the finite size of the transducer, and the influence of the fluid medium. Hence, the output response is corrected to account for these effects. The transfer function of the transducer is obtained from its data sheet, which is multiplied by the input pulse. The effect of the finite size of the source transducer is incorporated by using the radiation pattern of a flat piston transducer as discussed in [37], according to which

$$p_{\text{axial}} = p_0 e^{(-ikz)} \left( 1 - e^{\frac{-ika^2}{2z}} \right),$$
 (9)

also known as the Rayleigh-Sommerfield equation, where  $p_{\text{axial}}$  is the pressure along the acoustic axis of the transducer, while  $p_0$  is the pressure amplitude on the transducer surface, k is the wave number of the fluid medium, z is the axial distance from the center of the transducer along the acoustic axis, and a is the radius of the transducer. The fluid medium attenuates the wave propagation, which can be described by [38]:

$$p(z) = p_0 e^{-\alpha z},\tag{10}$$

where  $\alpha$  is the attenuation coefficient of the medium. In water,  $\alpha = 0.025 \, f^2/{\rm cm}$  at 20 °C, where f is the frequency in MHz. The central frequency  $f_c$ , BW, and Q factor of the IPUT are determined using its output response. The central frequency  $f_c = 0.604$  MHz is marked in Fig. 4(b), while its -6 dB BW is 60 kHz implying Q = 10.25.

#### 4.2. Laser wavelength sweep data

To get the RTF of the IPUT, we need to obtain its optical response. In the absence of an acoustical signal, we stepped the laser output wavelength from 1540 nm to 1550 nm with a 0.5 pm step and measured static optical transmissions for the MZI by a DC channel in digitizer. The actual MZI (Fig. 3(c)) has three output channels, of which the one where  $\frac{dT}{d\lambda}$  is maximum is used. Figure 5(a) shows the recorded voltage as a function of the wavelength, while Fig. 5(b) represents its zoomed-in view close to the measurement wavelength  $\lambda_m = 1544.13$  nm, where the red line is used to show the linear approximation of the responses of the IPUT. Using this line, the slope of the response is calculated as  $\left(\frac{dV}{d\lambda}\right) = -1.24$  V/nm. Noteworthy, the optical response depends on the optical modulation depth and the FSR and thus on the optical laser power. These values are later used in conjunction with the voltage sensitivity to obtain the total RTF of the IPUT. The voltage sensitivity is defined as the change in the output voltage in the receiver corresponding to the input pressure impinging on the IPUT. The input pressure is calculated by taking the voltage recorded at the clamps of the source transducer and correcting for the transmit transfer function, diffraction (9), and attenuation (10).

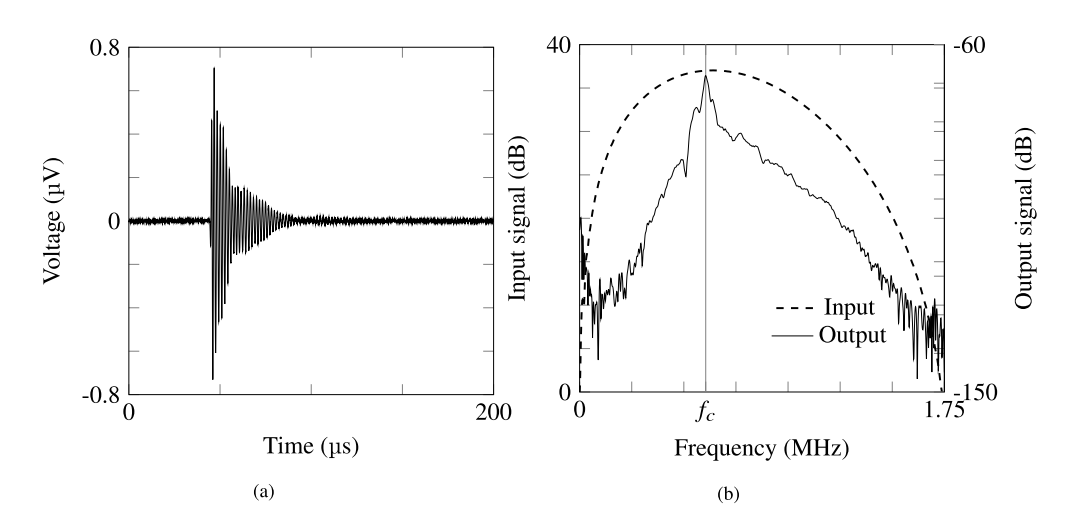


**Fig. 4.** (a) Input voltage of the digitizer obtained as an AC voltage as a function of time. (b) The supplied input (dashed) and recorded output (solid) spectra, with  $f_{\rm c1}=0.604$  MHz being the central frequency of the IPUT.

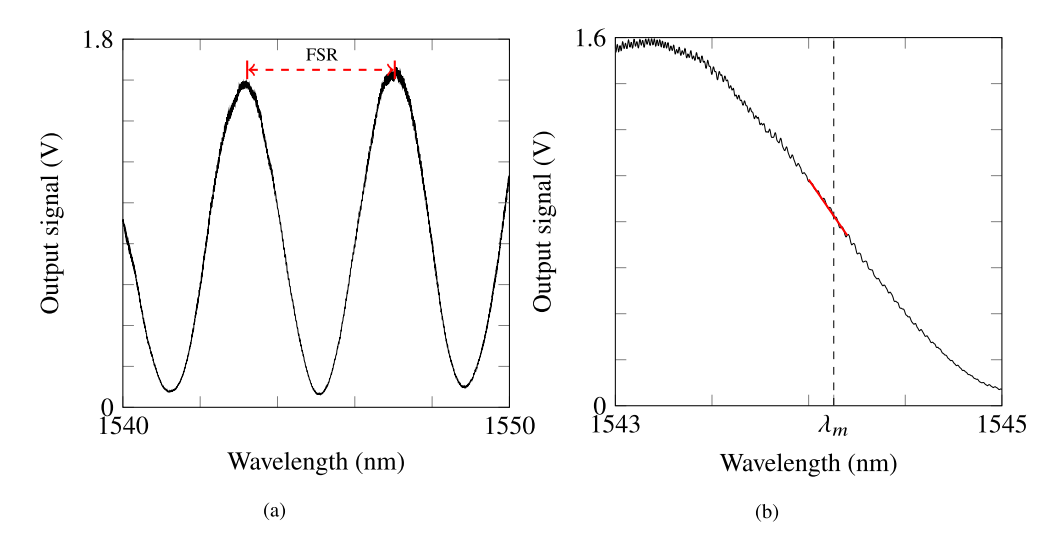


**Fig. 5.** Wavelength sweep of the IPUT: (a) DC input voltage of the digitizer as a function of the optical wavelength where FSR = 4 nm is marked (b) the spectral response between the wavelengths 1543 nm and 1545 nm where the slope of the channel (red line) is calculated corresponding to the measurement wavelength  $\lambda_m = 1544.13$  nm marked using black dashed line.

#### 4.3. Receive transfer function of the IPUT

The output spectrum shown in Fig. 4(b) is used to obtain the voltage sensitivity (in mV/Pa) of the IPUT, which is the AC response obtained at the digitizer in Fig. 2 after amplification (Gain = 10000 V/A)). The solid curve from Fig. 6(a) shows the sensitivity in mV/Pa of the IPUT with one membrane obtained by dividing the output spectrum (after correcting for the finite size of the transducer (refer Eq. (9)) and fluid attenuation (refer Eq. (10)) by the input spectrum. This response is a little noisy outside the sensitivity of the IPUT (<400 kHz and >800 kHz), while we see a response similar to the output signal from Fig. 4 close to  $f_{c1}$ . The sensitivity corresponding to  $f_{c1}$  is 0.66 mV/Pa. The RTF is the change in the wavelength of the laser through the MZI for a unit change in the applied pressure (refer to Eq. (6) in Section 2.1). It is determined by multiplying the voltage response  $(\frac{dV}{dP})$  with the wavelength sweep  $(\frac{dA}{dV})$  as follows:

$$\left(\frac{d\lambda}{dP}\right) = \left(\frac{dV}{dP}\right) \left(\frac{d\lambda}{dV}\right),\tag{11}$$

For the given IPUT,  $n_{\text{eff}} = 3.45$  (silicon). The resulting RTF is plotted using the solid curve in Fig. 6(b). The RTF corresponding to  $f_{c1}$  is 0.53 pm/Pa. We investigated the sensitivity and RTF of different IPUTs with multiple membranes, which is also discussed in the same figures (Figure 6(a) and Figure 6(b)). The IPUT with three membranes has a voltage sensitivity of 2 mV/Pa, while the five membrane IPUT has a sensitivity of 3.7 mV/Pa. Similarly, the RTF of the IPUT with the three membranes is 1.4 pm/Pa, whereas the five membrane IPUT's RTF is 2.24 pm/Pa. It is noteworthy that although the sensitivity and RTF response (in frequency) of three IPUT devices look similar, their resonance frequencies have small variations. As discussed already, the resonance frequency of IPUT with one membrane is  $f_{c1} = 0.605$  MHz, while the resonance frequency of three membrane IPUT is  $f_{c3} = 0.53$  MHz, and corresponding five membrane IPUT is  $f_{c5} = 0.52$  MHz. This deviation stems from the variations in the membrane geometries (thickness and diameter), primarily caused by the fabrication process (especially back-side etching of the membranes). Figure 7 shows the variation of RTF (corresponding to the resonance frequency) with respect to the number of membranes in the IPUT, which follows a linear response, implying that the increase in the number of membranes directly increases the RTF. The average value of RTF per membrane for all these IPUT chips is 0.47 pm/Pa, which is obtained from the slope of Fig. 7. This RTF is 7.1 times higher than a similar IPUT reported in the literature [17], while the IPUT with five membranes' RTF is 56 times higher, and since a higher RTF improves the sensitivity of the IPUT, our device performs favorably. Additionally, since the IPUT sensor (120 µm diameter) is very small compared to the acoustic wavelength in the fluid (2.5 mm), the sensor is almost omnidirectional (-6 dB opening angle from simulations is  $177.6^{\circ}$ ).

#### 4.4. Noise equivalent pressure of IPUTs

NEP is the lowest pressure amplitude the sensor can measure accurately. To determine the NEP, the amplitude of the excitation pulse is gradually varied, and the corresponding pressure from the IPUT is extracted. For the calculation, the time traces are filtered assuming the desired 100 % –6 dB BW of the resonance frequency of the IPUT. The result is shown in Figure 8 where 8(a), 8(b), and 8(c), respectively, represent the responses of one membrane IPUT, three membrane IPUT, and five membrane IPUT. Here the signal amplitude is represented as a function of the applied pressure, where the intersection of the signal (solid curve) and noise (dashed curve) provides us with the NEP. To that end the signal line is extended using a linear extrapolation. The resulting NEP for IPUT with one membrane is 42.5 mPa, IPUT with three membrane is 15.5 mPa, and IPUT with five membranes is 14.2 mPa. It is noteworthy, compared to the literature where the average NEP is 0.5 Pa, our IPUTs show a considerable improvement (11 to 35 times lower NEP) and hence enhancements in the sensitivity.

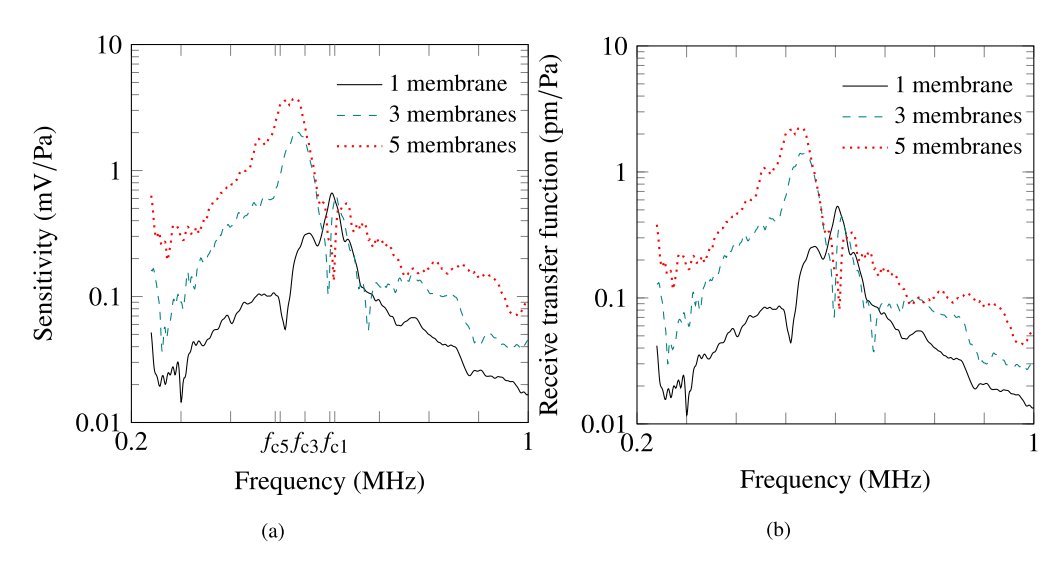


**Fig. 6.** Sensitivity and RTF as functions of the applied frequency for three different IPUTs: IPUT with a single membrane with resonance frequency  $f_{c1} = 0.604$  MHz, three membranes cascaded ( $f_{c3} = 0.53$  MHz), and five membranes cascaded ( $f_{c5} = 0.52$  MHz), respectively.

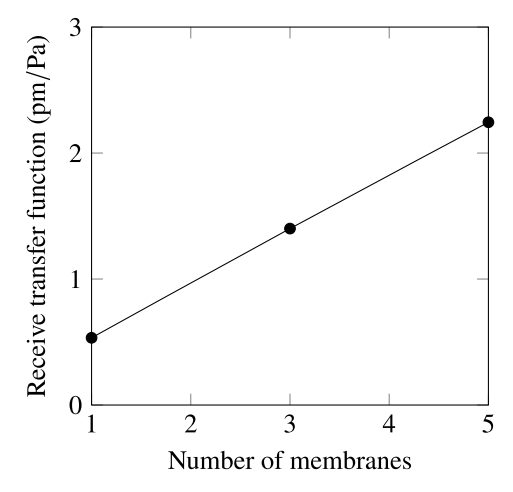


**Fig. 7.** RTFs corresponding to the resonance frequencies of the three IPUT devices follow a linear response.

## 5. Model results

## 5.1. Simulation settings

By using the time-domain finite element model (Comsol) explained in our previous article [33], we performed the dynamic analysis of the IPUT in water. The schematic of the model with geometric parameters and boundary conditions (BCs) is provided in Fig. 9. The properties considered in the model are listed in Table 1. The water domain considered here is vast compared to the IPUT (with a four-order difference between the water domain's height and membrane thickness), which limits the incoming plane wave reflections from the domain's edges and avoids overlapping of different time responses of the IPUT. A plane broadband ultrasound pulse with its center frequency close to 1 MHz and  $80\% -6 \, dB$  BW is applied on top of the water domain

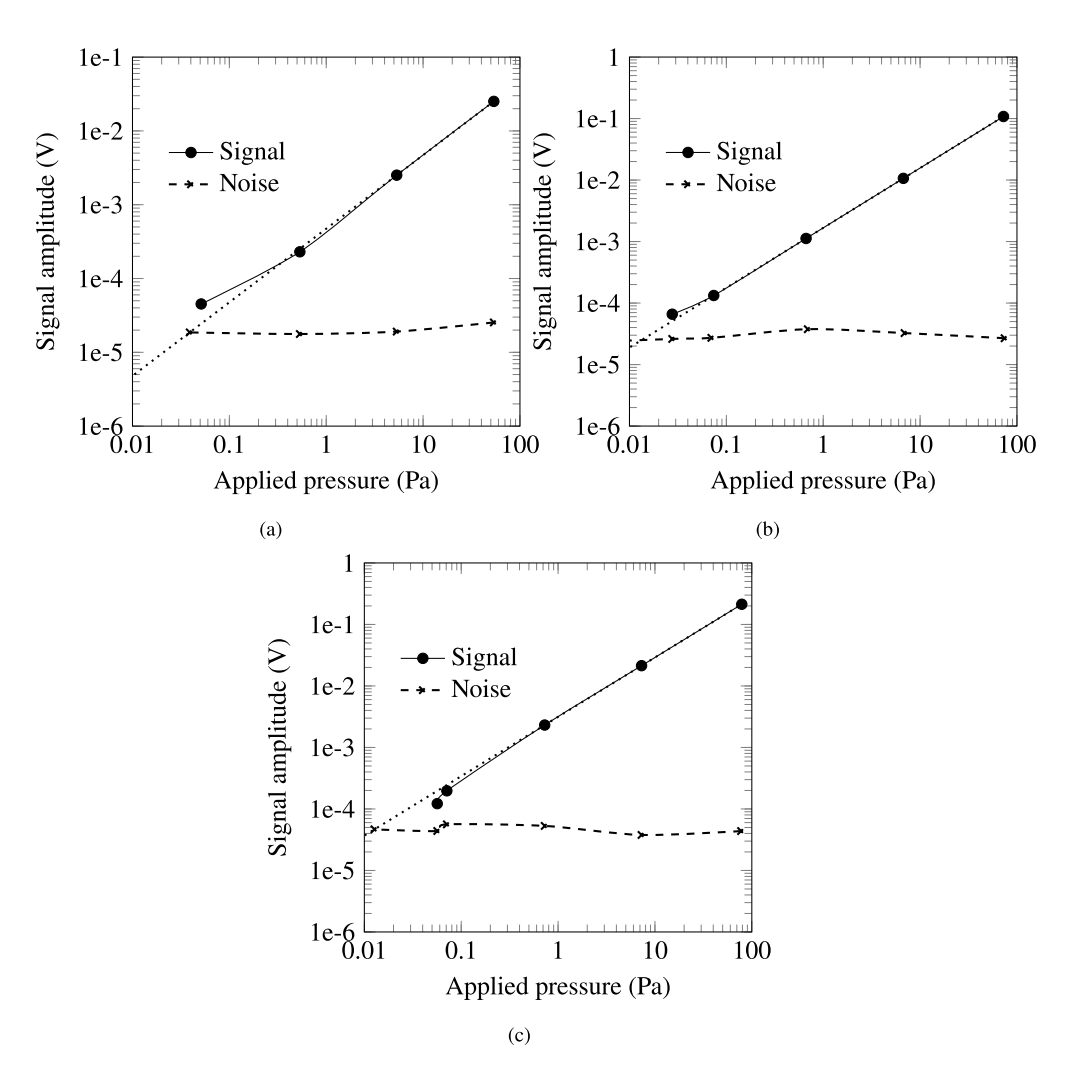


**Fig. 8.** Signal (solid line) and noise (dashed line) levels of the three different IPUTs for different applied acoustic peak pressures at the IPUT surface. The dotted lines extrapolate the signal to reach the noise levels. NEP of a single membrane IPUT is 42.5 mPa, IPUT with three membranes is 15.5 mPa and the IPUT with five membrane is 14.2 mPa.

(shown using a brown dashed line in the same figure), which excites the membrane primarily in its fundamental mode. We perform a time domain analysis for a total simulation time of  $60 \times T$ , with a time step of T/20, where T is the period of the pulse corresponding to the central frequency.

## 5.2. Time and frequency response of the membrane

The dynamic finite element model of the IPUT provides us with the acoustic response of the system. Then, the axial displacement of the membrane's center is extracted in the time domain as shown in Fig. 10(a). The response is very similar to that of a weakly-damped harmonic oscillator where the oscillations die out in around 20 cycles. By using FFT, we transform the time response to the frequency domain as shown in Fig. 10(b). Using this frequency response, the resonance frequency and Q-factor of the IPUT are determined. The frequency corresponding to the maximum signal amplitude is the resonance frequency of the membrane, which is obtained

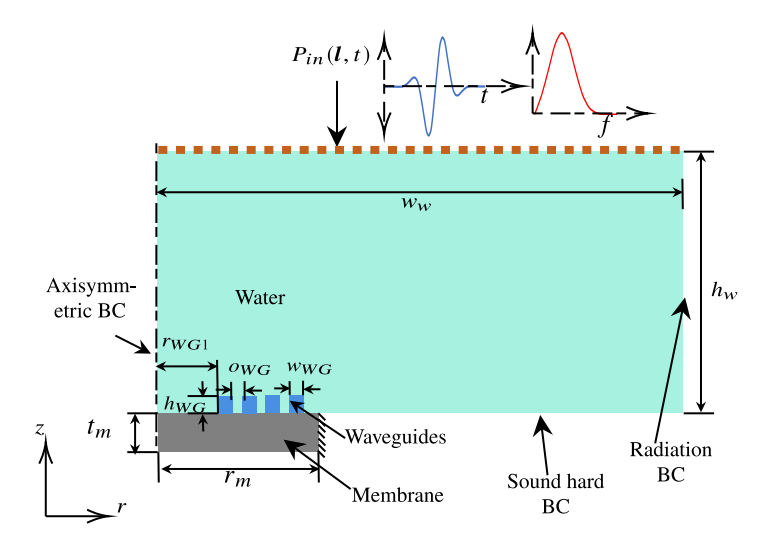


**Fig. 9.** Schematic of the finite element model of IPUT, where different geometric parameters and boundary conditions are marked. The dimensions of these geometric parameters are provided in Table 1.

Table 1. Properties of the IPUT and fluid used for simulation. Abbreviations –  $r_m$ : radius of the membrane,  $t_m$ : thickness of the membrane,  $h_{WG}$ : waveguide's height,  $w_{WG}$ : waveguide's width,  $r_{WG1}$ : radius of the first waveguide,  $o_{WG}$ : offset between the adjacent waveguides,  $h_w$ : height of the water domain,  $w_w$ : width of the water domain,  $\rho_m$ : membrane's density,  $\rho_w$ : density of water,  $\rho_{WG}$ : density of waveguide,  $E_m$ : elastic modulus of the membrane,  $K_w$ : bulk modulus of water,  $E_{WG}$ : elastic modulus of the waveguide,  $\nu_m$ : Poisson's ratio of the membrane, and  $\nu_{WG}$ : Poisson's ratio of the waveguide.

r <sub>m</sub>	t <sub>m</sub>	h <sub>WG</sub>	w <sub>WG</sub>	r <sub>WG1</sub>	owg	h <sub>w</sub>	$\mathbf{w}_{\mathbf{w}}$
μm	μm	μm	μm	μm	μm	mm	mm
60	3	3	2	30.47	3	30	60
$ ho_{ m m}$	$ ho_{ m w}$	$ ho_{ m WG}$	$E_{\rm m}$	$K_{\mathrm{w}}$	$E_{\mathrm{WG}}$	$\nu_{ m m}$	$\nu_{ m WG}$
$\rho_{\rm m}$ kg/m <sup>3</sup>	ρ <sub>w</sub> kg/m <sup>3</sup>	ρwG kg/m <sup>3</sup>	E <sub>m</sub> GPa	K <sub>w</sub> GPa	E <sub>WG</sub> GPa	ν <sub>m</sub>	ν <sub>WG</sub>

as  $f_c = 1.23$  MHz. The Q factor is calculated by dividing the frequency corresponding to the peak displacement by the BW corresponding to full-width half maximum (FWHM):

$$Q = \frac{f_c}{f_2 - f_1} = 8.45,\tag{12}$$

where  $f_1$  and  $f_2$  are the bounds of the -6 dB BW of the frequency response.

### 5.3. Receive transfer function of the IPUT sensor

The RTF is dominated by the waveguide elongation, and to calculate that, we need to obtain the physical length change of each waveguide. It is calculated via the radial displacement of each of the waveguides. To that end, the time response (similar to Fig. 10(a)) is extracted along the vertical edges of each of the waveguides. They are then transformed to the frequency domain just like in Fig. 10(b). The displacement values corresponding to  $f_c$  are then selected from the

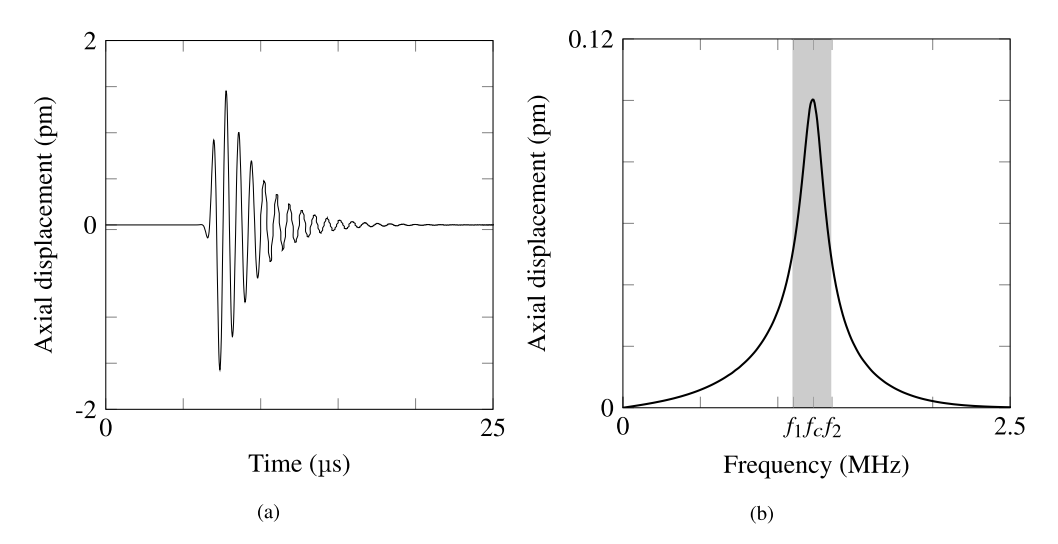


**Fig. 10.** The axial displacement of the membrane is represented as functions of (a) time and (b) frequency. The indicated frequencies correspond to the peak displacement ( $f_c = 1.23 \text{ MHz}$ ), and the lower ( $f_1 = 1.15 \text{ MHz}$ ) and upper ( $f_2 = 1.3 \text{ MHz}$ ) bounds of the -6 dB BW (shaded region).

frequency response. The variations of this displacement with the height of the waveguide is plotted in Fig. 11. For clarity, the figure only shows the displacements along the left edges of each of the waveguides. Since the waveguides are narrow compared to the membrane's diameter (see Table 1), the displacements would not experience much variation along the width of the waveguide. We can observe that the displacements of all waveguides increase with increasing waveguide thickness and with increasing distance from the membrane center (along the radial direction). Here waveguide 4, being the furthest from the center of the IPUT, where axisymmetric BC is provided (see the inset of Fig. 11), showed the largest variation in the radial displacement. Moreover, all waveguides exhibit mostly linear response in their radial displacements along their height, implying that the waveguides themselves do not experience significant bending.

Since each waveguide contributes to the total physical length change of the spiral, the individual radial displacements from Fig. 11 are used to calculate the corresponding RTF for which  $n_{\rm eff}$  and  $n_g$  are needed. They can be obtained for the Si waveguide where the propagation of the light is limited to its fundamental mode via an optical mode solver. Here we used FIMMWAVE [39] to obtain  $n_{\rm eff}=3.43$  and  $n_g=3.645$ , which are used along with the displacements from Fig. 11, along with  $\lambda=1550$  nm, and dP=0.0148 Pa (amplitude of the pressure pulse at  $f_c$ ) to obtain the RTF<sub>el</sub> due to the wavelength shift as follows.

$$RTF_{el} = \sum_{i=1}^{4} RTF_i = 0.09 pm/Pa$$
 (13)

We can observe that the dynamic response predicted by the model is much different than the experiment. The resonance frequency and Q factor, respectively, are two times higher and 18% lower than the experimental results. Additionally, the RTF is 4.5 times lower than the experiments. We believe these variations are majorly due to the influence of geometric variations and prestress experienced by the membrane.

## 5.4. Influence of geometric variation in the IPUT's behavior

Since the fabricated IPUT has variations in thickness due to over-etching, we updated the model with the actually measured membrane thickness (2.42 µm, measured via reflectometry

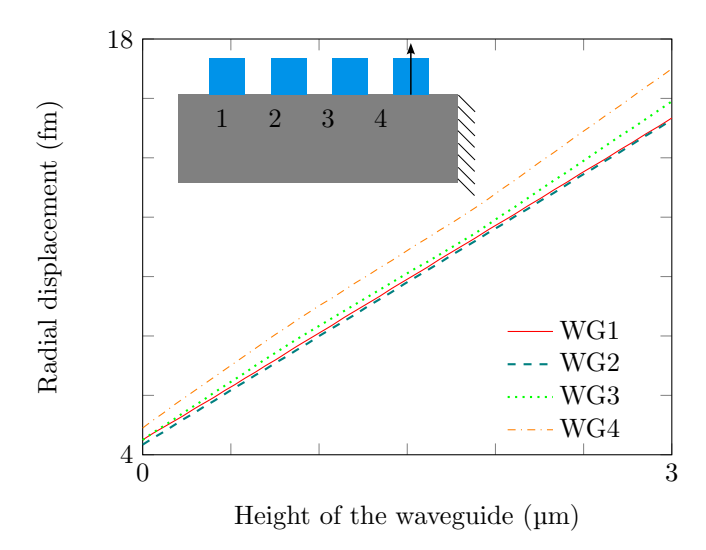


**Fig. 11.** Computed radial displacement along the height of all 4 waveguides. The inset shows the schematic of the waveguides and the membrane region where the arrow goes through the center of the last waveguide represents the abscissa. Waveguides ranging from 1 to 4 are also marked here. The black arrow represents the direction along which the displacements are extracted.

and calibrated confocal microscope) and performed the dynamic analysis as described earlier. The resulting frequency response of the IPUT's axial displacement is shown in Fig. 12(a). The resonance frequency of the new IPUT model is  $f_c^g = 0.98$  MHz, which is 20% lower than the IPUT with initial geometry (1.23 MHz). Similarly, the new Q factor is 8.8, which is 12% higher than the previous IPUT model (8.45). Now, we proceed to calculate the RTF of the new geometry using the radial displacement of all 4 waveguides shown in Fig. 12(b). The reduction in resonance frequency and increase (slight) in the Q factor resulted in an increase in the absolute radial displacement of all waveguides. Due to this, the total RTF also increased from 0.09 pm/Pa (initial IPUT geometry) to 0.11 pm/Pa (new geometry) which is 22%. Compared to the experimental results, the model with the new geometry still suffers from considerable deviations. For instance, the resonance frequency is 60% higher, while the Q factor is 16% lower for the model compared to the experiments. Additionally, the RTF is still 3.7 times lower than the experiments.

#### 5.5. Influence of prestress in the IPUT's response

As discussed previously, prestress developed due to the fabrication process (e.g., cooling after the deposition process yields thermal stress) greatly influences the behavior of IPUTs [22]. Here we investigate whether the prestress would significantly modify the parameters of the IPUT. To that end, we perform the dynamic analysis of the IPUT (with the updated geometry) where the effects of prestress are incorporated as a constant initial stress of  $-250\,\mathrm{MPa}$  (compressive), which is typical for the current silicon-on-insulator device [40] along the radial and angular directions. The prestress is implemented in the Comsol model, where the initial stress attribute is added to the solid mechanics module, while the geometric nonlinearity is enabled in the solution step. The remaining boundary conditions are kept the same as the previous models (see Fig. 9). The resulting displacement response of the IPUT in the frequency domain is plotted in Fig. 13(a). Here the shaded region shows the  $-6\,\mathrm{dB}$  BW bounded by  $f_1^p = 0.575\,\mathrm{MHz}$  and  $f_2^p = 0.625\,\mathrm{MHz}$ , while the resonance frequency,  $f_c^p = 0.6\,\mathrm{MHz}$ . The resulting Q factor is 12. Due to including prestress, the natural frequency of the model gets very close to the experimental value with only

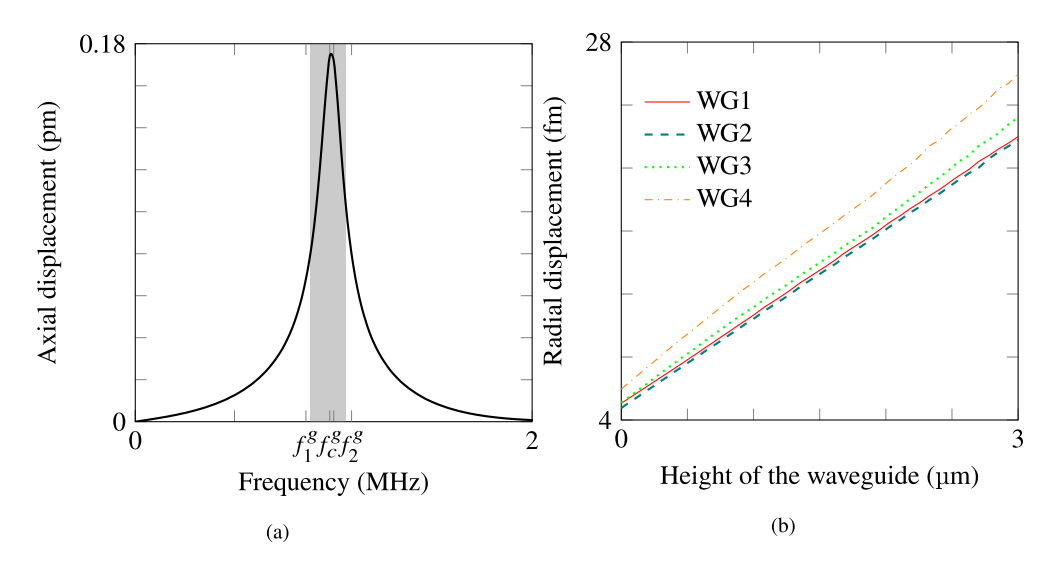


**Fig. 12.** (a) The axial displacement of the IPUT incorporating geometric variations versus frequency, where the indicated frequencies correspond to the peak displacement ( $f_c^g = 0.98$  MHz), and the lower ( $f_1^g = 0.88$  MHz) and upper ( $f_2^g = 1.04$  MHz) bounds of the -6 dB BW. (b) Radial displacement at the resonance frequency for all 4 waveguides.

2% variation. The difference in the Q factor is a little more than that of frequency, which is 14% higher than the experimental value. Figure 13(b) shows the radial displacement of all waveguides, which is more than twice that of the model without prestress. The resulting RTF is 0.46 pm/Pa, which is only 2% lower than the corresponding experimental value of 0.47 pm/Pa (the average RTF value for several IPUT chips see Section 4.3).

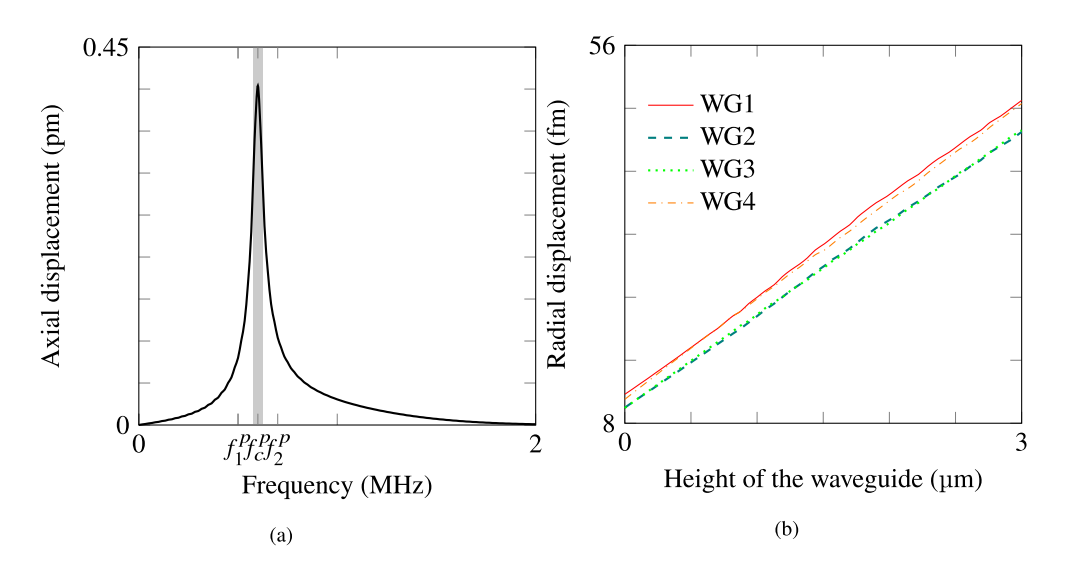


**Fig. 13.** (a) The axial displacement of the IPUT incorporating geometric variations and prestress ( $-250 \,\mathrm{MPa}$ ) versus frequency, where the indicated frequencies correspond to the peak displacement ( $f_c^p = 0.6 \,\mathrm{MHz}$ ), and the lower ( $f_1^p = 0.575 \,\mathrm{MHz}$ ) and upper ( $f_2^p = 0.625 \,\mathrm{MHz}$ ) bounds of the  $-6 \,\mathrm{dB}$  BW. (b) Radial displacement at the resonance frequency for all 4 waveguides.

## 6. Summary and conclusion

In this work, we validated the semi-analytical model that describes the dynamic response of an IPUT proposed in our previous work experimentally, and improved it by incorporating geometric and prestress aspects. Underwater ultrasound experiments of IPUTs were performed to obtain their resonance frequency, Q factor, and receive transfer function. Then, by using the finite element method, we model the dynamic behavior of the IPUT in the time domain, from which the IPUT's resonance frequency, Q factor, and waveguides' elongations are extracted. These parameters aid in predicting the receive transfer function of the IPUT. The resonance frequency, Q-factor, and the receive transfer function predicted by the initial model were considerably different than the experiments. To address this, the model was updated with the actual geometry of the fabricated IPUT and prestress experienced by the SiO<sub>2</sub> membrane. Thus, we were able to bring the parameters close to the experiment where the difference in the resonant frequency was only 2%, while the Q factor differed by 14%. The receive transfer function predicted by the model with prestress is only 2.5 % lower than the experiment, which is an excellent match. Thus, it is essential to incorporate the influences of prestress in the IPUT model to predict its dynamic response accurately. Additionally, we investigated the noise performance of the IPUT by determining the noise equivalent pressure (NEP) and found that our IPUT has very low NEP: 42.5 mPa compared to 500 mPa of the state of the art ultrasound sensors. We further extended the study by testing different IPUT devices with multiple membranes and found that with the increase in the number of membranes, the RTF increases linearly, and the NEP decreases. Thus, by cascading multiple membranes we can drastically improve the sensitivity of the IPUT and can be applied for highly sensitive applications. A possible future direction would be to investigate the influence of prestress and its variations on the dynamic behavior of IPUTs so that we can make accurate model predictions and use prestress as a design parameter.

**Funding.** Nederlandse Organisatie voor Wetenschappelijk Onderzoek (NWA-1160.18.095); HORIZON CL4-2022-DIGITAL-EMERGING-01 (101100633).

**Acknowledgments.** The authors greatly appreciate the support from VTT Finland in fabricating the specimens and CITC Netherlands for packaging the optical chips.

**Disclosures.** The authors declare no conflict of interest.

Data Availability. Data underlying the results are available from the corresponding author upon request.

#### References

- K. Santhi, "A survey on medical imaging techniques and applications," J. Innov. Image Process. 4(3), 173–182 (2022).
- 2. T. L. Szabo, Diagnostic ultrasound imaging: inside out (Academic press, 2004).
- 3. G. Muehllehner and J. S. Karp, "Positron emission tomography," Phys. Med. Biol. 51(13), R117–R137 (2006).
- 4. M. T. Vlaardingerbroek and J. A. Boer, *Magnetic resonance imaging: theory and practice* (Springer Science & Business Media, 2013).
- B. He and D. Wu, "Imaging and visualization of 3-d cardiac electric activity," IEEE Trans. Inform. Technol. Biomed. 5(3), 181–186 (2001).
- 6. D. H. Brooks, "Medical imaging modalities," IEEE Signal Process. Mag. 14(1), 20 (1997).
- 7. S. Stocker, "Medical imaging apparatus," (2016). US Patent 9,451,902.
- 8. S. Lalitha, T. Sanjana, H. Bhavana, *et al.*, "Medical imaging modalities and different image processing techniques: State of the art review," Disruptive Developments in Biomedical Applications pp. 17–36 (2022).
- A. Manbachi and R. S. C. Cobbold, "Development and application of piezoelectric materials for ultrasound generation and detection," Ultrasound 19(4), 187–196 (2011).
- A. K. Ilkhechi, C. Ceroici, Z. Li, et al., "Transparent capacitive micromachined ultrasonic transducer (cmut) arrays for real-time photoacoustic applications," Opt. Express 28(9), 13750–13760 (2020).
- 11. J. Jung, W. Lee, W. Kang, *et al.*, "Review of piezoelectric micromachined ultrasonic transducers and their applications," J. Micromech. Microeng. **27**(11), 113001 (2017).
- B. Zeqiri, "Exposure criteria for medical diagnostic ultrasound: Ii. criteria based on all known mechanisms: (ncrp report no. 140) national council on radiation protection and measurements (ncrp), 2002," Ultrasound Med. Biol. 29(12), 1809 (2003).
- W. Xia, D. Piras, J. C. G. van Hespen, et al., "An optimized ultrasound detector for photoacoustic breast tomography," Med. Phys. 40(3), 032901 (2013).
- R. Manwar, K. Kratkiewicz, and K. Avanaki, "Overview of ultrasound detection technologies for photoacoustic imaging," Micromachines 11(7), 692 (2020).
- 15. P. R. Saulson, "Thermal noise in mechanical experiments," Phys. Rev. D 42(8), 2437–2445 (1990).
- W. J. Westerveld, M. Mahmud-Ul-Hasan, R. Shnaiderman, et al., "Sensitive, small, broadband and scalable optomechanical ultrasound sensor in silicon photonics," Nat. Photonics 15(5), 341–345 (2021).
- 17. S. M. Leinders, W. J. Westerveld, J. Pozo, *et al.*, "A sensitive optical micro-machined ultrasound sensor (omus) based on a silicon photonic ring resonator on an acoustical membrane," Sci. Rep. 5(1), 14328 (2015).
- 18. J. A. Guggenheim, J. Li, T. J. Allen, *et al.*, "Ultrasensitive plano-concave optical microresonators for ultrasound sensing," Nat. Photonics **11**(11), 714–719 (2017).
- 19. R. Shnaiderman, G. Wissmeyer, O. Ülgen, *et al.*, "A submicrometre silicon-on-insulator resonator for ultrasound detection," Nature **585**(7825), 372–378 (2020).
- B. Ouyang, Y. Li, M. Kruidhof, et al., "On-chip silicon mach-zehnder interferometer sensor for ultrasound detection," Opt. Lett. 44(8), 1928–1931 (2019).
- R. J. J. van Gulik, B. M. de Boer, and P. J. Harmsma, "Refractive index sensing using a three-port interferometer and comparison with ring resonators," IEEE J. Sel. Top. Quantum Electron. 23(2), 433–439 (2017).
- 22. G. J. Hornig, K. G. Scheuer, E. B. Dew, *et al.*, "Ultrasound sensing at thermomechanical limits with optomechanical buckled-dome microcavities," Opt. Express **30**(18), 33083–33096 (2022).
- H. Yang, Z.-G. Hu, Y. Lei, et al., "High-sensitivity air-coupled megahertz-frequency ultrasound detection using on-chip microcavities," Phys. Rev. Appl. 18(3), 034035 (2022).
- H. Yang, X. Cao, Z.-G. Hu, et al., "Micropascal-sensitivity ultrasound sensors based on optical microcavities," arXiv (2022).
- E. Epp, N. Ponnampalam, W. Newman, et al., "Hollow bragg waveguides fabricated by controlled buckling of si/sio2 multilayers," Opt. Express 18(24), 24917–24925 (2010).
- J. Sun, F. Hou, S. Feng, et al., "Integrated optical microrings on fiber facet for broadband ultrasound detection," Adv. Sens. Res. 3(12), 2400076 (2024).
- 27. H. Fan, L. Zhang, S. Gao, *et al.*, "Ultrasound sensing based on an in-fiber dual-cavity fabry–perot interferometer," Opt. Lett. **44**(15), 3606–3609 (2019).
- 28. B. Ouyang, Y. Li, M. Kruidhof, et al., "Highly sensitive silicon Mach-Zehnder interferometer-based ultrasound sensor," in *Integrated Optics: Devices, Materials, and Technologies XXIV*, vol. 11283 S. M. García-Blanco and P. Cheben, eds., International Society for Optics and Photonics (SPIE, 2020), p. 112830R.
- S. M. Leinders, W. J. Westerveld, J. Pozo, et al., "Design and characterization of a sensitive optical micro-machined ultrasound transducer," J. Acoust. Soc. Am. 137(4\_Supplement), 2426 (2015).

- 30. S. Tsesses, D. Aronovich, A. Grinberg, *et al.*, "Modeling the sensitivity dependence of silicon-photonics-based ultrasound detectors," Opt. Lett. **42**(24), 5262–5265 (2017).
- 31. V. Rochus, R. Jansen, J. Goyvaerts, et al., "Design of a mzi micro-opto-mechanical pressure sensor for a sin photonics platform," in 2016 17th International Conference on Thermal, Mechanical and Multi-Physics Simulation and Experiments in Microelectronics and Microsystems (EuroSimE), (2016), pp. 1–5.
- 32. V. Rochus, R. Jansen, J. Goyvaerts, *et al.*, "Fast analytical model of mzi micro-opto-mechanical pressure sensor," J. Micromech. Microeng. **28**(6), 064003 (2018).
- 33. S. V. Valappil, P. Harmsma, M. van der Heiden, *et al.*, "Semi-analytical modeling of receive transfer function and thermal noise of integrated photonic ultrasound transducers," (2025).
- 34. G. T. Reed and A. P. Knights, Silicon photonics: an introduction (John Wiley & Sons, 2004).
- 35. P. L. van Neer, H. J. Vos, and N. de Jong, "Reflector-based phase calibration of ultrasound transducers," Ultrasonics 51(1), 1–6 (2011).
- 36. T. Aalto, M. Harjanne, and M. Cherchi, "VTT's micron-scale silicon rib+strip waveguide platform," in *Silicon Photonics and Photonic Integrated Circuits V*, vol. 9891 L. Vivien, L. Pavesi, and S. Pelli, eds., International Society for Optics and Photonics (SPIE, 2016), p. 98911G.
- X. Chen, K. Q. Schwarz, and K. J. Parker, "Radiation pattern of a focused transducer: A numerically convergent solution," J. Acoust. Soc. Am. 94(5), 2979–2991 (1993).
- 38. R. S. Cobbold, Foundations of biomedical ultrasound (Oxford university press, 2006).
- "Mode Solvers Waveguide CAD Software FIMMWAVE photond.com," https://www.photond.com/products/fimmwave.htm. [Accessed 03-10-2024].
- E. Kobeda and E. A. Irene, "SiO<sub>2</sub> film stress distribution during thermal oxidation of Si," J. Vac. Sci. & Technol. B: Microelectron. Process. Phenom 6(2), 574–578 (1988).